J. Fluid Mech. (2006), *vol.* 548, *pp.* 403–430. © 2006 Cambridge University Press
doi:10.1017/S0022112005007809 Printed in the United Kingdom

On phase transition in compressible flows: modelling and validation

By XISHENG LUO[1]†, BART PRAST[2], M. E. H. VAN DONGEN[1], H. W. M. HOEIJMAKERS[1] AND JIMING YANG[3]

[1]Department of Applied Physics, Eindhoven University of Technology, Eindhoven, The Netherlands
[2]TWISTER BV, The Netherlands
[3]Department of Modern Mechanics, University of Science and Technology of China, Hefei, China

(Received 18 August 2004 and in revised form 2 August 2005)

A physical model for compressible flows with phase transition is described, in which all the processes of phase transition, i.e. nucleation, droplet growth, droplet evaporation and de-nucleation, are incorporated. The model is focused on dilute mixtures of vapour and droplets in a carrier gas with typical maximum liquid mass fraction smaller than 0.02. The new model is based on a reinterpretation of Hill's method of moments of the droplet size distribution function. Starting from the general dynamic equation, it is emphasized that nucleation or de-nucleation correspond to the rates at which droplets enter or leave droplet size space, respectively. Nucleation and de-nucleation have to be treated differently in agreement with their differences in physical nature. Attention is given to the droplet growth model that takes into account Knudsen effects and temperature differences between droplets and gas. The new phase transition model is then combined with the Euler equations and results in a new numerical method: ASCE2D. The numerical method is first applied to the problem of shock/expansion wave formation in a closed shock tube with humid nitrogen as a driver gas. Nucleation and droplet growth are induced by the expansion wave, and in turn affect the structure of the expansion wave. When the main shock, reflected from the end wall of the low-pressure section, passes the condensation zone, evaporation and de-nucleation occur. As a second example, the problem of the flow of humid nitrogen in a pulse-expansion wave tube, designed to study nucleation and droplet growth in monodisperse clouds, is investigated experimentally and numerically.

1. Introduction

When a humid gas undergoes a fast expansion, the mixture may attain a state of supersaturation and, as a consequence, droplets are formed, which will grow or shrink and disappear, depending on the flow characteristics. If the expansion is sufficiently strong, droplets will be formed directly from the vapour phase, a process known as homogeneous nucleation (Abraham 1974; Kashchiev 2000). An important aspect of the condensation process is the release of latent heat. Adding heat to a flow at transonic velocities, may have a strong impact on the flow, for example resulting in condensation-induced flow instabilities (see Wegener & Cagliostro 1973; Sislian & Glass 1976; Sichel 1981; Matsuo *et al.* 1983, 1985; Adam & Schnerr

† Present address: Shock wave laboratory, RWTH-Aachen, 52062, Aachen, Germany. xLuo@swl.rwth-aachen.de.

https://doi.org/10.1017/S0022112005007809 Published online by Cambridge University Press

1997; Delale, Lamanna & van Dongen 2001). Condensation phenomena are observed above the suction side of wings in transonic flight and in wing-tip vortices. They are found in steam turbines, in supersonic windtunnels, and in high-pressure pipelines after the sudden opening of pressure relief valves. Gasdynamic facilities such as Laval nozzles and expansion wave tubes offer excellent possibilities for studying the physics of droplet formation and droplet growth, and determining nucleation rates for gas/vapour mixtures in a wide range of pressure, temperature and supersaturation (Looijmans & van Dongen 1997; Peeters, Hrubý & van Dongen 2001*a*; Peeters, Gielis & van Dongen 2002).

In the literature, effects of phase transition in unsteady flows have been studied in detail, including theoretical, experimental and numerical approaches. A review can be found in Adam & Schnerr (1997) and Luo & van Dongen (2003). Related numerical studies on the evaporation of droplets in turbulent flows have been reported by Mashayek (1998) and Miller & Bellan (1999).

The present study is focused on condensation and evaporation phenomena in dilute mixtures of vapour, droplets and a carrier gas with typical maximum liquid mass fractions of the order of 0.01. The droplets to be considered remain small with a typical maximum diameter of 1 μm. The generation, transport and growth of droplets is described by the conservation laws for a finite number of moments of the droplet size distribution function. The method of moments is commonly used in work on aerosol behaviour in the earth's atmosphere and in aerosol reactors. Hill (1966) introduced this method for the study of nozzle flows with condensation. Hill's method consists of tracking the evolution in time and space of a small number of (low-order) moments of the droplet size distribution. Subject to certain assumptions, it appears to be possible to give a full description of the condensation processes in terms of transport equations for the first four moments of the size distribution function. Many numerical studies based on this method have been reported. Brown, Rubin & Biswas (1995) applied this method incorporating the effects of nucleation, condensation, coagulation, diffusion, inertial impaction and thermophoresis in combination with a RANS (Reynolds averaged Navier–Stokes) method to two-dimensional axi-symmetric and three-dimensional flows including the flow in a nozzle. Mundinger's work (Mundinger 1994) is also based on this method in combination with the Euler equations. Prast (1997) developed a computational method to simulate supersonic nozzle flows with condensation based on the work of Mundinger. Put *et al.* (2001, 2002) and Put (2003) extended this method including real gas effects.

Most of these numerical methods are able to describe nucleation and condensation phenomena in unsteady flows, but they ignore the disappearance of droplets owing to evaporation, which may occur when the droplet cloud is compressed or heated, e.g. when a strong shock wave passes the condensation zone. This de-nucleation has to be accounted for, because otherwise erroneous heterogenous condensation will take place in subsequent expansions of the flow. In order to overcome this difficulty, an extension of Hill's method of moments has been proposed (Luo & van Dongen 2003), in which the processes of phase transition including de-nucleation are incorporated. In the present study, we consider the underlying physical principles in more detail.

This paper is organized as follows. In § 2, the nucleation theory is briefly described and some basic concepts such as saturation ratio and critical droplet size are given. Then the droplet growth model is discussed with emphasis on the calculation of the temperature of the droplet. In § 3, starting from the general dynamic equation, the extended method of moments of the size distribution function is developed. In § 4, the set of governing equations of the gas/vapour–droplet mixture is obtained

https://doi.org/10.1017/S0022112005007809 Published online by Cambridge University Press

by combining the method of moments of the size distribution function with the Euler equations. Section 4 also specifies the equation of state of the gas/vapour–droplet mixture and briefly describes the new numerical method, i.e. an adaptive solver for condensation and evaporation, which implements the new physical model. Section 5 demonstrates the effects of phase transition on the flow field by numerically simulating the flow in a closed shock tube with humid nitrogen. Section 6 is devoted to the experimental and numerical study of the flow in a so-called pulse-expansion wave tube, which forms the test case for the validation of the present physical model. Conclusions are drawn in § 7.

2. Nucleation theory and droplet growth

2.1. *Nucleation theory*

For vapour–liquid phase equilibrium, the vapour pressure p_v is equal to the saturated vapour pressure p_s, which is, in a one-component system, a function of temperature only: $p_s = p_s(T)$. If a vapour is in a supersaturated state, $p_v > p_s$, droplets will be formed such that the system tends to a new equilibrium. The non-equilibrium parameter for an ideal vapour is the saturation ratio S, defined as:

$$S = p_v / p_s(T). \tag{2.1}$$

Vapour–liquid equilibrium for a droplet of radius r is different from vapour–liquid equilibrium near a flat interface. This is due to the surface tension, which causes the pressure inside a droplet to exceed the pressure outside the droplet.

For a droplet with radius r in a metastable equilibrium state, we then find the so-called Kelvin expression (Sonntag, Borgnakke & van Wylen 1998):

$$\frac{p_v^{eq}}{p_s} = \exp\left(\frac{v_{ml} 2\sigma}{r R_m T}\right) = \exp(Ke), \tag{2.2}$$

where superscript '*eq*' denotes the equilibrium state and the Kelvin number is defined as $Ke = v_{ml} 2\sigma / r R_m T$ with σ the surface tension, v_{ml} the molar liquid volume and R_m the universal gas constant.

From (2.2), we see that the equilibrium vapour pressure is related to the size of the droplet. For a given uniform vapour pressure, $p_v > p_s$, and for a cloud of droplets with a wide range of sizes, there exists a metastable equilibrium for one particular droplet size: $p_v = p_v^{eq} = S p_s$. Inserting this into (2.2) we find the critical size for a droplet r^*:

$$r^* \equiv \frac{2\sigma v_{ml}}{R_m T \ln S}. \tag{2.3}$$

Droplets with size $r > r^*$ will tend to grow. Droplets with $r < r^*$ are subsaturated and tend to disappear. Droplets with size r^* are called critical droplets.

The homogeneous nucleation rate is defined as the rate at which critical droplets are able to catch additional vapour molecules and in this way pass the energy barrier ΔG^* for the formation of stable droplets. The value of this energy barrier reads:

$$\Delta G^* = \frac{\hat{v}_{ml}^2}{(k_B T)^2 (\ln S)^2} \frac{16\pi}{3} \sigma^3, \tag{2.4}$$

with $\hat{v}_{ml}$ the molecular volume, k_B the Boltzmann constant $k_B = R_m / N_A$ where N_A is Avogadro's number.

https://doi.org/10.1017/S0022112005007809 Published online by Cambridge University Press

For the nucleation rate, expressions are found of the form:

$$J = K \exp(-\Delta G^*/k_B T). \tag{2.5}$$

The factor K is called the kinetic prefactor. We specify here two different expressions for this kinetic prefactor (Kashchiev 2000):

$$K_{CNT} = S\frac{p_s^2}{(k_B T)^2}\hat{v}_{ml}\left(\frac{2\sigma N_A}{\pi m}\right)^{1/2}, \tag{2.6}$$

with m the molar mass, which corresponds to the classical nucleation theory (CNT)†, and

$$K_{ICCT} = K_{CNT}\exp\left(\frac{\sigma a_0}{k_B T}\right), \tag{2.7}$$

with $a_0 = (36\pi)^{1/3}\hat{v}_{ml}^{2/3}$, which is referred to as the internally consistent classical nucleation theory (ICCT). ICCT is implemented in the present numerical method.

2.2. *Droplet growth*

Once a stable cluster has been formed, it will grow into a droplet, suspended in the carrier gas–vapour mixture. The process that governs the growth depends to a large extent on the Knudsen number Kn. This dimensionless group is defined as the ratio of the mean free path l of a vapour molecule and the droplet diameter $2r$: $Kn = l/2r$, where the mean free path is given by $l = 2\mu\sqrt{RT}/p$, with μ the dynamic viscosity of the gas mixture, R the specific gas constant of the mixture, T the temperature of the gas/vapour and p the pressure of the mixture. For small Kn, i.e. relatively large droplets, droplets are growing by vapour molecules diffusing to the droplet surface in a more or less continuous way. This is called the continuum regime or the diffusion-controlled regime. For large Kn, i.e. small droplets, the growth is controlled by the kinetic process of impingement of vapour molecules from the surrounding mixture onto the droplet. This is the free molecular regime. Thus, a growth model applicable from the moment of nucleation (nm-scale) to the time the droplets have grown to μm scale should cover the whole range of Knudsen numbers.

There exist many approximate theories to describe droplet growth with dependence on the Knudsen-number as discussed, by among others, Miller, Harstad & Bellan (1998) and Peeters, Luijten & van Dongen (2001*b*). Based on an accurate experimental validation, Peeters *et al.* (2001*b*) have compared the Gyarmathy model (Gyarmathy 1982) and the more sophisticated model of Young (1993). Because the Gyarmathy model performs reasonably well for the whole Knudsen domain investigated, and because of its simple form, we have implemented this model. It expresses the growth rate at intermediate Kn numbers in terms of the growth rates in the two limiting cases of $Kn \ll 1$ and $Kn \to \infty$. In the continuum limit, the driving force for droplet growth in a dilute gas/vapour mixture is the difference between the vapour pressure at the surface p_v^{eq} and the vapour pressure in the bulk p_v. The vapour at the droplet surface is assumed to be in local phase equilibrium with the droplet at temperature T_d. However, since latent heat is released or absorbed owing to the phase transition process, the droplet temperature is governed by the exchange of latent heat between droplet and surrounding gas. In the so-called quasi-steady wet-bulb approximation, there is a simple relation between the mass flow from the droplet to the environment

† In CNT, the original expression for K contains a factor S^2. Nowadays (Oxtoby 1992), it is generally accepted that the correct factor is S.

https://doi.org/10.1017/S0022112005007809 Published online by Cambridge University Press

$\dot{M}$ and the heat flow from the droplet to the environment $\dot{H}$:

$$\dot{H} = -\dot{M}L, \tag{2.8}$$

with L the latent heat.

Droplet mass and heat flows can be described in a rather general form, including effects of Knudsen numbers and of convection in a formal way by means of the Nusselt numbers Nu_M and Nu_H. We then write $\dot{M}$ and $\dot{H}$ as:

$$\left.\begin{aligned} \dot{M} &= 4\pi r^2 Nu_{\dot{M}} \frac{(p_v^{eq} - p_v)}{p} \frac{D_{mod}}{2r}, \\ \dot{H} &= 4\pi r^2 Nu_{\dot{H}} (T_d - T) \frac{k_m}{2r}, \end{aligned}\right\} \tag{2.9}$$

where D_{mod} is the modified diffusion coefficient, defined as $D_{mod} = D_m p/(R_v T_m)$ with R_v the specific gas constant of the vapour. The thermal conductivity k_m, and the binary diffusion coefficient D_m are evaluated at the intermediate temperature T_m, defined as (Hubbard, Denny & Mills 1975):

$$T_m = \tfrac{1}{3}(2T_d + T). \tag{2.10}$$

The Nusselt numbers depend on the Knudsen number and on the relative Reynolds number referring to the slip velocity between droplets and carrier gas. We shall assume here that there is no slip between droplets and carrier gas, which is a valid assumption if the Stokes number, $St = \tau_d/\tau_f$, is sufficiently small. The droplet momentum relaxation time for Stokes flow τ_d is equal to $2r^2\rho_l/9\mu$, while τ_f is the characteristic time for the rate of change of flow momentum. For the small droplets we consider, $r \leqslant 0.5\,\mu\text{m}$, and typical values for τ_f of $1\,\mu\text{s}$, the Stokes number is much smaller than unity. Then, the Nusselt numbers depend only on the Knudsen number. The Nusselt numbers for the two limiting regimes and the one for the transition regime (without slip, dilute mixtures) are specified in Appendix B.

Equations (2.8) and (2.9) result in an implicit formula to calculate the droplet temperature T_d:

$$Nu_{\dot{H}} k_m (T - T_d) = -Nu_{\dot{M}} L(T_d) D_{mod} \frac{p_v - p_v^{eq}}{p}. \tag{2.11}$$

The droplet growth rate can then be expressed either by the energy conservation law or by the mass conservation law:

$$\frac{\mathrm{d}r^2}{\mathrm{d}t} = \frac{Nu_{\dot{H}}^{tr} k_m}{\rho_l L}(T_d - T) = -\frac{Nu_{\dot{M}}^{tr} D_{mod}}{\rho_l} \frac{p_v - p_v^{eq}}{p_a}, \tag{2.12}$$

where superscription '*tr*' denotes variables evaluated using the expressions in the transition regime, subscription '*a*' denotes the carrier gas and ρ_l is the density of liquid water.

2.3. *Explicit method for* T_d

To obtain the droplet temperature T_d, the quasi-steady wet-bulb equation, (2.11) has to be solved. It can be solved accurately by an iterative method. Unfortunately, since (2.11) has to be solved for each point in the flow, this evaluation is expensive in terms of computing time. Therefore explicit approximate expressions have been proposed by several authors (Mason 1953; Gyarmathy 1963; Wagner 1982; Barrett & Clement 1988). Smolders (1992) evaluated these explicit models and concluded that Gyarmathy's model gives the best results and also formulated a second-order

https://doi.org/10.1017/S0022112005007809 Published online by Cambridge University Press

correction to the Gyarmathy model:

$$\left(\frac{T_d}{T}-1\right)=f(S,Ke)[C_1+C_2]^{-1}(1-\delta_1), \tag{2.13}$$

where

$$\delta_1 \approx \frac{\frac{1}{2}C_1^2-C_2}{(C_1+C_2)^2}(\ln S-Ke), \tag{2.14}$$

$$f(S,Ke)=\ln S-Ke,$$

$$C_1=\frac{T}{\theta S}\left(\frac{p}{p_s}-S\right),$$

$$C_2=\frac{L}{R_v T},$$

with $\theta = D_{mod}LNu_M^{tr}/(k_m Nu_E^{tr})$.

We assessed the accuracy of the explicit expression (2.13) comparing it to the solution of the implicit expression (2.11) for processes including evaporation ($S<1$). It is found that for the strong evaporation associated with strong shock waves, adopting the implicit method is mandatory since the explicit method causes large errors ($>10\%$) in estimating the temperature of the droplets T_d. For lower temperatures and higher saturation ratios, it appears that using the implicit method is again inevitable. More details can be found in Appendix C. In the present study, the flow conditions are such that the use of the explicit method is allowed.

3. The extended method of moments

It was recently shown by Hagmeijer (2004) that Hill's moment equations, to describe nucleation and droplet growth processes, can be derived from the so-called general dynamic equation (GDE, Friedlander 1977). In this section, we shall derive a generalized version of Hill's moment equations, also starting from the GDE, describing both condensation and evaporation processes.

3.1. *Size distribution function and moment method*

Generally, a droplet cloud can be characterized by its size distribution function f defined such that $f(r;\boldsymbol{x},t)$ gives the number density of particles with radius between r and $r+\mathrm{d}r$ at time t at position $\boldsymbol{x}$. The droplet number density $n_d(\boldsymbol{x},t)$ is defined as the number of droplets per unit volume exceeding a certain minimum radius r_b, which is generally a function of space and time, i.e. $r_b = r_b(\boldsymbol{x},t)$, and will be specified later:

$$n_d(\boldsymbol{x},t)=\int_{r_b}^{\infty} f(r;\boldsymbol{x},t)\,\mathrm{d}r. \tag{3.1}$$

In a well-mixed fluid, $f(r;\boldsymbol{x},t)$ satisfies an equation known as the GDE, which describes the evolution of the size distribution in time when the particles undergo condensational growth, removal and coagulation. We consider the motion of non-slipping droplets that experience condensation/evaporation only. In that case, the GDE reduces to:

$$\frac{\partial f}{\partial t}+\nabla\cdot(f\boldsymbol{v})+\frac{\partial}{\partial r}\left(f\frac{\mathrm{d}r}{\mathrm{d}t}\right)=0. \tag{3.2}$$

The mass-averaged velocity is denoted by $\boldsymbol{v}$ and $\mathrm{d}r/\mathrm{d}t$ is the Lagrangian growth rate of a droplet owing to condensation or evaporation. When condensation or evaporation

https://doi.org/10.1017/S0022112005007809 Published online by Cambridge University Press

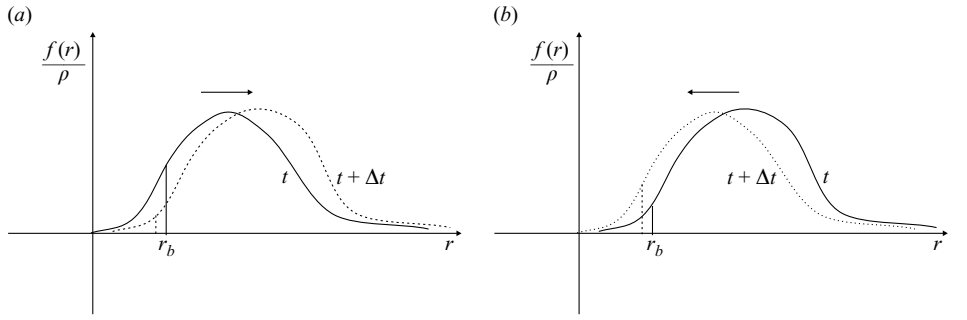


FIGURE 1. The shift of the size distribution function in size space due to (*a*) condensation or (*b*) evaporation. r_b denotes the lower bound of the droplet radius. Note r_b is also changing during condensation or evaporation.

takes place, the size distribution per unit mass, $f(r)/\rho$, will shift in size space, as shown in figure 1. Here, ρ is the density of the mixture.

The so-called moment equations are obtained by multiplying (3.2) by r^n and then integrating over r from r_b to infinity, which yields:

$$\int_{r_b}^{\infty} \frac{\partial}{\partial t}(r^n f)\,\mathrm{d}r + \int_{r_b}^{\infty} \nabla\cdot(r^n f \boldsymbol{v})\,\mathrm{d}r = f_b r_b^n \left(\frac{\mathrm{d}r}{\mathrm{d}t}\right)_b + \int_{r_b}^{\infty} n f r^{n-1}\frac{\mathrm{d}r}{\mathrm{d}t}\,\mathrm{d}r, \tag{3.3}$$

with r_b the lower bound of the size distribution function, f_b the value of the size distribution function at r_b, and $(\mathrm{d}r/\mathrm{d}t)_b$ the growth rate at r_b. Since $r_b = r_b(\boldsymbol{x}, t)$, the left-hand side can be rewritten as:

$$\frac{\partial}{\partial t}\int_{r_b}^{\infty} r^n f\,\mathrm{d}r + \nabla\cdot\int_{r_b}^{\infty} r^n f \boldsymbol{v}\,\mathrm{d}r + r_b^n f_b \frac{\partial r_b}{\partial t} + r_b^n f_b \boldsymbol{v}\cdot\nabla r_b. \tag{3.4}$$

The last two terms are equal to $r_b^n f_b \mathrm{d}r_b/\mathrm{d}t$ with $\mathrm{d}r_b/\mathrm{d}t$ the rate of change of the lower bound r_b when moving with the mass element. Therefore, (3.3) can be rewritten as:

$$\frac{\partial}{\partial t}\int_{r_b}^{\infty} f r^n \mathrm{d}r + \nabla\cdot\left[\boldsymbol{v}\left(\int_{r_b}^{\infty} f r^n \mathrm{d}r\right)\right] = f_b r_b^n\left[\left(\frac{\mathrm{d}r}{\mathrm{d}t}\right)_b - \frac{\mathrm{d}r_b}{\mathrm{d}t}\right] + \int_{r_b}^{\infty} n f r^{n-1}\frac{\mathrm{d}r}{\mathrm{d}t}\,\mathrm{d}r. \tag{3.5}$$

The last term in (3.5) can be approximated as $n(\overline{\mathrm{d}r}/\mathrm{d}t)\int_{r_b}^{\infty} f r^{n-1}\,\mathrm{d}r$ with $\overline{\mathrm{d}r}/\mathrm{d}t$ an average growth rate, i.e.

$$\overline{\frac{\mathrm{d}r}{\mathrm{d}t}} = \frac{\displaystyle\int_{r_b}^{\infty}\frac{\mathrm{d}r}{\mathrm{d}t} f(r)\,\mathrm{d}r}{\displaystyle\int_{r_b}^{\infty} f(r)\,\mathrm{d}r}. \tag{3.6}$$

Here, it is assumed that the growth rate $(\mathrm{d}r/\mathrm{d}t)$ is independent of r, or weakly depending on r, which is certainly valid in the Hertz–Knudsen regime ($Kn > 2$), neglecting the so-called Kelvin effect (Gyarmathy 1982).

Introducing the moment Q_n as:

$$\rho Q_n = \int_{r_b}^{\infty} r^n f\,\mathrm{d}r, \tag{3.7}$$

we then have:

$$\frac{\partial}{\partial t}(\rho Q_n) + \nabla\cdot(\rho Q_n \boldsymbol{v}) = n\overline{\frac{\mathrm{d}r}{\mathrm{d}t}}\rho Q_{n-1} + f_b r_b^n\left[\left(\frac{\mathrm{d}r}{\mathrm{d}t}\right)_b - \frac{\mathrm{d}r_b}{\mathrm{d}t}\right]. \tag{3.8}$$

https://doi.org/10.1017/S0022112005007809 Published online by Cambridge University Press

Following Hill, a full set of equations is obtained by combining the first four moment equations ($n=0$, 1, 2, 3) with the conservation laws of total mass, momentum and energy for the whole mixture. In the present study, we use the liquid mass fraction g, defined as the ratio of the mass of the liquid droplets M_l and the mass of the mixture M, instead of the third-order moment Q_3. According to the definition of Q_3 and g, they are directly related through $g=4\pi\rho_l Q_3/3$.

3.2. *Physical model for condensation*

If the saturation ratio $S>1$, the condensation process dominates. In this case, new droplets are formed which enter the size space by crossing the lower boundary r_b at the so-called critical radius r^*. At the same time, the size distribution function will shift to the right.

From the definition of the moments, the zeroth-order moment Q_0 is equal to the number density of droplets per unit mass n_d/ρ and therefore Q_0 is fully determined by the nucleation rate J_n:

$$\frac{\partial}{\partial t}(\rho Q_0)+\nabla\cdot(\rho Q_0\boldsymbol{v})=J_n. \tag{3.9}$$

Thus, the nucleation rate J_n can be identified as:

$$J_n\equiv f_b\left[\left(\frac{\mathrm{d}r}{\mathrm{d}t}\right)_b-\frac{\mathrm{d}r_b}{\mathrm{d}t}\right]. \tag{3.10}$$

It is a positive quantity that can be directly derived from nucleation theory. The lower bound r_b is just the critical radius r^*: $r_b\equiv r^*$.

Then the four moment equations are identical with the original moment equations of Hill for nucleation and condensation (Hill 1966).

3.3. *Physical model for evaporation*

If the saturation ratio $S<1$, then the evaporation process takes over and $\mathrm{d}r/\mathrm{d}t<0$. In this case, the droplets will cross the lower bound r_b and disintegrate into vapour molecules. This implies that the number density and the median size of the droplets will decrease, so the size distribution function will shift to the left. We define the de-nucleation rate J_{dn} for $S<1$ as:

$$J_{dn}\equiv f_b[(\mathrm{d}r/\mathrm{d}t)_b-\mathrm{d}r_b/\mathrm{d}t]. \tag{3.11}$$

To evaluate J_{dn}, however, we have to find an estimate of f_b and of $[(\mathrm{d}r/\mathrm{d}t)_b-\mathrm{d}r_b/\mathrm{d}t]$, which means that we have to adopt a lower bound of the radius r_b and a distribution function f in size space. For simplicity, we first take the radius r_b to be constant, equal to zero. Therefore, $[(\mathrm{d}r/\mathrm{d}t)_b-\mathrm{d}r_b/\mathrm{d}t]$ reduces to $(\mathrm{d}r/\mathrm{d}t)_0$ and J_{dn} is defined as $f_0(\mathrm{d}r/\mathrm{d}t)_0$ with subscript '0' referring to $r_b=0$. In order to proceed, we need information on the size distribution function f at the onset of evaporation. Although this knowledge is available in principle through the moments of the size distribution function, we choose here a more practical approach. The shape of the size distribution function is assumed to have a certain form, characterized by a parameter vector S_P. For example, the shape of a normalized Gaussian distribution is fully determined by its variance σ_d. The values of the shape parameters follow from the moments of f. Since the droplet growth rate is assumed to be independent of droplet radius, following the path of a mass element, the size distribution function f/ρ shifts undistorted to smaller radii. We shall refer to the properties of this undistorted size distribution at the onset of evaporation as the onset number density $n_d^o=(n_d/\rho)^o$ and as the onset

https://doi.org/10.1017/S0022112005007809 Published online by Cambridge University Press

Case	f	S_P	f_0
Top-hat	$\begin{cases} \dfrac{\rho n_{d0}}{(r_2 - r_1)}, & r \in (r_1, r_2); \\ 0, & r \notin (r_1, r_2), \end{cases}$	$\sqrt{\dfrac{3Q_2}{10Q_0} + \dfrac{9Q_3}{10Q_1} - \dfrac{6Q_1^2}{5Q_0^2}}$	$\begin{cases} \dfrac{\rho n_{d0}^o}{2S_P^o}, & r_m < S_P^o; \\ 0, & r_m \geqslant S_P^o, \end{cases}$
Gaussian	$\dfrac{\rho n_{d0}}{\sqrt{2\pi}\sigma_d} \exp\left(-(r - r_m)^2/2\sigma_d^2\right)$	$\sqrt{\dfrac{Q_2^2 - Q_1 Q_3}{Q_0 Q_2 - 2Q_1^2}}$	$\dfrac{\rho n_{d0}^o}{\sqrt{2\pi}S_P^o} \exp[-2\left(r_m/2S_P^o\right)^2]$

TABLE 1. Examples for the shape parameter and f_0 using a top-hat and a Gaussian size distribution function, respectively. r_m denotes the modal radius. It should be noted that the vector S_P contains only one element in these two examples.

shape vector S_P^o with superscript 'o' referring to the onset of evaporation. Since the size distribution $f(r)/\rho$ keeps its shape, n_d^o and S_P^o are constants along a Lagrangian trajectory as long as evaporation occurs. In Eulerian notation we have:

$$\left.\begin{aligned} \frac{\partial}{\partial t}\left(\rho n_d^o\right) + \nabla \cdot \left(\rho n_d^o \boldsymbol{v}\right) = 0, \\ \frac{\partial}{\partial t}\left(\rho S_P^o\right) + \nabla \cdot \left(\rho S_P^o \boldsymbol{v}\right) = 0. \end{aligned}\right\} \tag{3.12}$$

In order to specify fully the shifting size distribution function that preserves its shape, we introduce first the modal radius at the onset of evaporation r_m^0. The 'position' of the distribution function in size space is then fully defined by r_m^c which satisfies:

$$r_m^c = r_m^o + \int_{t_0}^{t} \overline{\frac{\mathrm{d}r}{\mathrm{d}t}}\, \mathrm{d}t, \tag{3.13}$$

where integration refers to a Lagrangian trajectory and t_0 refers to the moment evaporation starts. Now the de-nucleation rate J_{dn} can be expressed as:

$$J_{dn} = f_0 \overline{\frac{\mathrm{d}r}{\mathrm{d}t}}, \tag{3.14}$$

where f_0 is determined from the size distribution function with the known parameters n_d^o, S_P^o and r_m^c. This enables us to evaluate the right-hand side of (3.8).

As examples, the shape parameter and the corresponding f_0 for a top-hat and a Gaussian size distribution function are given in table 1. For the top-hat function, the shape parameter is defined here as the half-width of the size distribution function, which is determined by the upper and lower radii, r_1 and r_2. For the Gaussian distribution function, the shape parameter is set equal to the standard variance σ_d. Detailed descriptions about the model based on these two size distribution functions can be found in Luo & van Dongen (2003) and Luo (2004).

4. Governing equations and numerical method

The fluid dynamical behaviour of the two-phase system of gas/vapour and droplets is described by the system of conservation equations, Euler or Navier–Stokes, supplemented with the model for phase transition. Combining the moment equations of the size distribution with the Euler equations for time-dependent two-dimensional flow, the governing equation for the complete system can be written in the vectorial

https://doi.org/10.1017/S0022112005007809 Published online by Cambridge University Press

form:

$$\frac{\partial \boldsymbol{U}}{\partial t} + \frac{\partial \boldsymbol{F}}{\partial x} + \frac{\partial \boldsymbol{G}}{\partial y} = \boldsymbol{S}, \tag{4.1}$$

where $\boldsymbol{U}$ is the vector of unknowns, $\boldsymbol{F}$ and $\boldsymbol{G}$ represent the convective fluxes in the x- and y-direction, respectively, and $\boldsymbol{S}$ is the source term:

$$\boldsymbol{U} = \begin{pmatrix} \rho \\ \rho u \\ \rho v \\ \rho E \\ \rho g \\ \rho Q_2 \\ \rho Q_1 \\ \rho Q_0 \end{pmatrix}; \quad \boldsymbol{F} = \begin{pmatrix} \rho u \\ \rho u^2 + p \\ \rho uv \\ (\rho E + p)u \\ \rho gu \\ \rho Q_2 u \\ \rho Q_1 u \\ \rho Q_0 u \end{pmatrix}; \quad \boldsymbol{G} = \begin{pmatrix} \rho v \\ \rho uv \\ \rho v^2 + p \\ (\rho E + p)v \\ \rho gv \\ \rho Q_2 v \\ \rho Q_1 v \\ \rho Q_0 v \end{pmatrix}, \tag{4.2}$$

$$\boldsymbol{S} = \begin{pmatrix} 0 \\ 0 \\ 0 \\ 0 \\ \frac{4}{3}\pi\rho_l \left(J r_b^3 + 3\rho Q_2 \overline{\frac{\mathrm{d}r}{\mathrm{d}t}} \right) \\ J r_b^2 + 2\rho Q_1 \overline{\frac{\mathrm{d}r}{\mathrm{d}t}} \\ J r_b + \rho Q_0 \overline{\frac{\mathrm{d}r}{\mathrm{d}t}} \\ J \end{pmatrix},$$

where E is the total energy per unit mass of mixture, u and v the velocity in the x- and y-direction, respectively.

The first four components of the source term are zero, since we consider conservation laws for the mixture of gas, vapour and droplets as a whole. When the saturation ratio S is larger than unity, the nucleation theory is employed to determine the nucleation rate J. In that case, the lower bound r_b equals the critical radius r^*, which follows from nucleation theory as well. Where S is less than unity, the evaporation model is used to evaluate the de-nucleation rate J, while the lower bound r_b is set equal to zero.

4.1. *Thermodynamic properties*

We shall assume the vapour to be a calorically perfect gas and the latent heat to be a linear function of temperature. In that case, the temperature of the gas/vapour T, the pressure of the mixture p and the frozen sound speed of the mixture c_f can be related to the internal energy per unit mass of the mixture e (consisting of contributions from the three components, i.e. the carrier gas, the vapour and the liquid) and the liquid mass fraction g according to Mundinger (1994):

$$T = \frac{e + gL_0}{C_{v0} + g_0 C_{vv} + g(R_v - L_1)}, \tag{4.3}$$

$$p = \rho \frac{e + gL_0}{C_{v0} + g_0 C_{vv} + g(R_v - L_1)} [R_0 - (g - g_0)R_v], \tag{4.4}$$

https://doi.org/10.1017/S0022112005007809 Published online by Cambridge University Press

$$c_f^2 = \frac{p}{\rho}\frac{C_{p0} + g_0 C_{pv} - gL_1}{C_{v0} + g_0 C_{vv} + g(R_v - L_1)}, \tag{4.5}$$

with C_{v0} and C_{p0} the initial specific heats at constant density and pressure of the mixture, respectively, R_0 the initial gas constant of the mixture, and g_0 the initial liquid mass fraction. The latent heat has been linearized, $L = L_0 + L_1 T$, at a reference temperature.

It should be noted that in (4.3) the difference between droplet temperature and gas temperature has been neglected, which is a good approximation for the dilute mixtures considered. The internal energy per unit mass e relates to the total energy per unit mass E as:

$$e = E - \tfrac{1}{2}(u^2 + v^2). \tag{4.6}$$

All the physical parameters and the physical properties of the mixtures considered in the present study are given in Appendix A.

4.2. *Adaptive solver for condensation and evaporation: ASCE2D*

The extended nucleation/condensation model has been implemented in a numerical method. Based on the fractional-step-method (Oran & Boris 1987), the governing equations are split in two parts: the homogeneous part without source terms and the inhomogeneous part with the source terms due to phase transition, i.e.

$$\frac{\partial \boldsymbol{U}^{hom}}{\partial t} + \frac{\partial \boldsymbol{F}}{\partial x} + \frac{\partial \boldsymbol{G}}{\partial y} = 0, \tag{4.7}$$

$$\frac{\partial \boldsymbol{U}}{\partial t} = \boldsymbol{S}(\boldsymbol{U}^{hom}). \tag{4.8}$$

The homogeneous part is solved by applying the same method as used in VAS2D developed by Sun (1998) and Sun & Takayama (1999) for compressible flows. For the inhomogeneous part, the treatment by Mundinger (1994) and Prast (1997) is followed. The combination of the two methods has been developed into a new numerical method: ASCE2D (two-dimensional and axi-symmetric adaptive solver for condensation and evaporation). The finite-volume method is used to discretize the conservation laws by applying them directly to each non-overlapping control volume. The MUSCL-Hancock scheme (van Leer 1984), a second-order upwind scheme has been adopted to compute the flux through the cell interface. In the new method, the equations have been discretized on an unstructured quadrilateral mesh that adapts to the time-dependent flow. The adaptation criterion uses the maximum of the error sensor of the density and the two velocity components. Our experience so far is that the method can handle all important physical phenomena in compressible flows, such as expansion waves, shock waves, contact surfaces and vortices.

The treatment of boundary conditions is similar to that of VAS2D, i.e. image cells are used for solid wall boundaries or symmetry lines, such that the normal component of the velocity vanishes. For a detailed description of the implementation of the boundary conditions and of the accuracy of this method, see Sun (1998) and Luo (2004).

We shall first study the problem of the flow in a closed shock tube, with humid nitrogen as the driver gas, in which the effect of phase transition is demonstrated clearly. Then the flow in a pulse-expansion wave tube, with helium as the carrier gas, used for determining nucleation rates and droplet growth rates, is investigated experimentally and numerically in detail to validate the present method.

https://doi.org/10.1017/S0022112005007809 Published online by Cambridge University Press

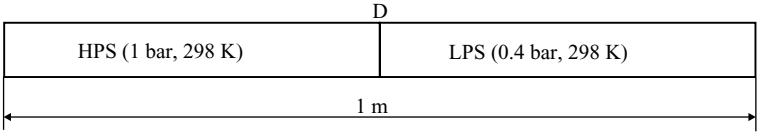


FIGURE 2. Sketch of the closed shock tube. The shock tube has a total length of 1 m and a diaphragm D initially divides it into two equal parts, the high-pressure section (HPS) and the low-pressure section (LPS). The tube is filled with either dry nitrogen or humid nitrogen (initial saturation ratio of 0.8 in the HPS and of 0.32 in the LPS).

5. Phase transition in a closed shock tube

The numerical method is applied to the expansion and compression of humid nitrogen in a closed shock tube, as shown in figure 2. The shock tube has a total length of 1 m and is divided into two equal parts initially separated by a diaphragm D. Initial pressures chosen are 1 bar and 0.4 bar in the high-pressure section (HPS) and the low-pressure section (LPS), respectively. The temperature of the gas in both sections is 298 K. The tube is filled with either dry nitrogen or humid nitrogen (initial saturation ratio of 0.8 in the HPS and of 0.32 in the LPS). A top-hat size distribution function is employed to evaluate the de-nucleation rate (using a Gaussian distribution function yields results that are only slightly different). Results for humid nitrogen are compared with results for dry nitrogen.

After removal of the diaphragm, an instantaneous local pressure equilibration occurs which leads to the formation of a right-running shock wave and a right-running contact surface. At the same time, an expansion fan propagates to the left into the HPS and causes the density of the gas to decrease. Figure 3 shows space–time diagrams of density contours for the dry and humid nitrogen case. The shock wave reflects at the endwall of the LPS and the reflected shock interacts with the contact surface, which results in a weak shock wave travelling to the right and a transmitted shock wave continuing to the left. Then the shock wave encounters the expansion wave reflected from the endwall of the HPS, which complicates the flow field further. This problem exhibits several interactions of nonlinear waves: the shock wave, the reflected shock wave at the LPS, the re-reflected shock wave at the HPS endwall, the contact surface (only mildly smeared), the expansion wave, the reflected expansion wave at the HPS endwall and the re-reflected expansion wave at the LPS endwall. The interactions between these waves are captured by the present numerical method, which demonstrates that the method can handle all important interactions in compressible flows. In the humid nitrogen case, the fast expansion causes homogeneous nucleation and subsequently droplet growth. Owing to the latent heat release during the condensation, a pressure wave is generated, which affects the nucleation process and results in a distortion of the expansion fan. On the other hand, the shock reflected from the endwall of the LPS passes the condensation zone and causes evaporation. Therefore, both condensation and evaporation occur in this relatively simple configuration. The wave pattern is more complex in the humid nitrogen case than that in the dry nitrogen case owing to the latent heat released to, or absorbed from, the flow during phase transition. To demonstrate the effect of phase transition on the flow field, results of temperature and pressure are shown for times 2.5 and 6.5 ms.

As shown in figure 4 for $t = 2.5$ ms, the homogeneous nucleation and condensation process causes a higher pressure level in the reflected expansion wave and a steepening of the pressure distribution, leading to a weak condensation shock. Owing to the latent

https://doi.org/10.1017/S0022112005007809 Published online by Cambridge University Press

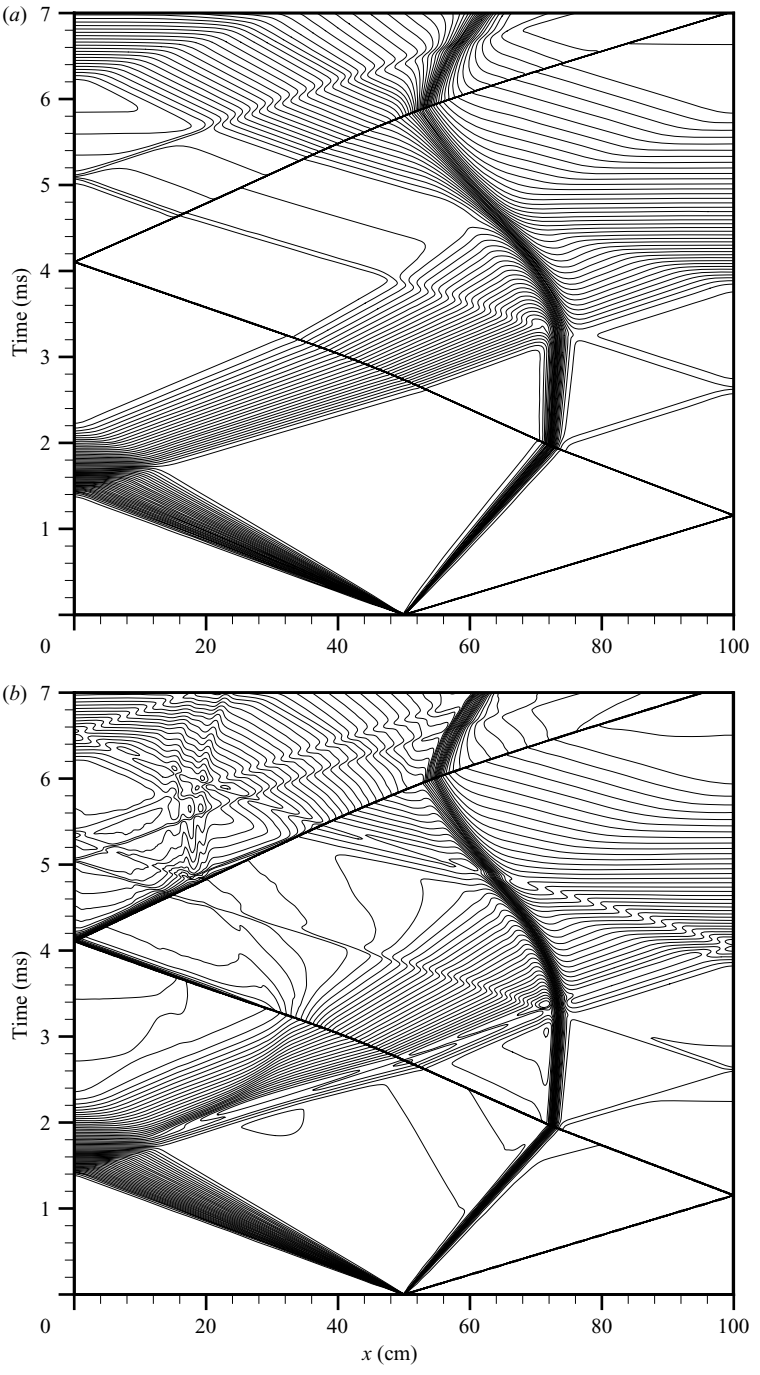


FIGURE 3. Density contours for the closed shock tube problem in a space–time diagram in (*a*) dry and (*b*) humid nitrogen. Initial pressures are 1 bar and 0.4 bar in the high-pressure (HPS) and low-pressure sections (LPS), respectively, at a temperature of 298 K. The initial saturation ratio in the HPS for the humid case is 0.8. The density range is from 0.45 to 1.17 $\mathrm{kg\,m^{-3}}$ with a contour increment of 0.01 $\mathrm{kg\,m^{-3}}$.

https://doi.org/10.1017/S0022112005007809 Published online by Cambridge University Press

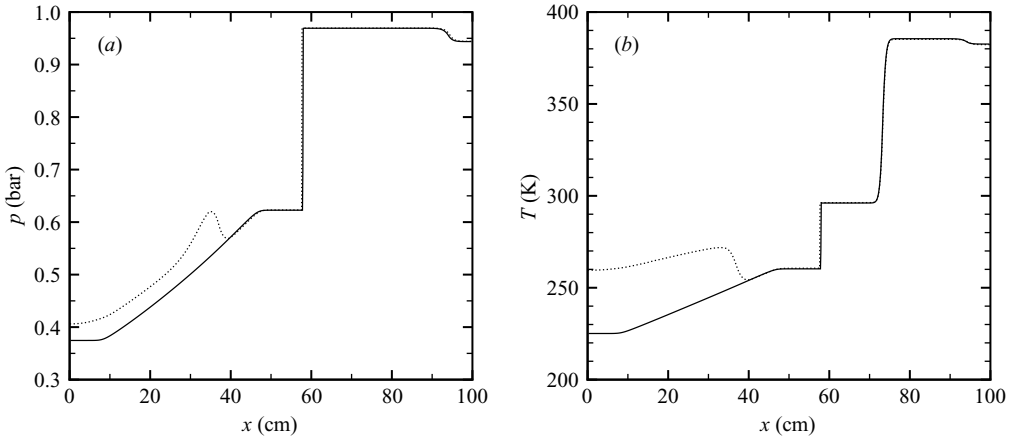


FIGURE 4. (*a*) The pressure and (*b*) the temperature profiles along the tube at 2.5 ms. Dry nitrogen: solid line; humid nitrogen: dotted line.

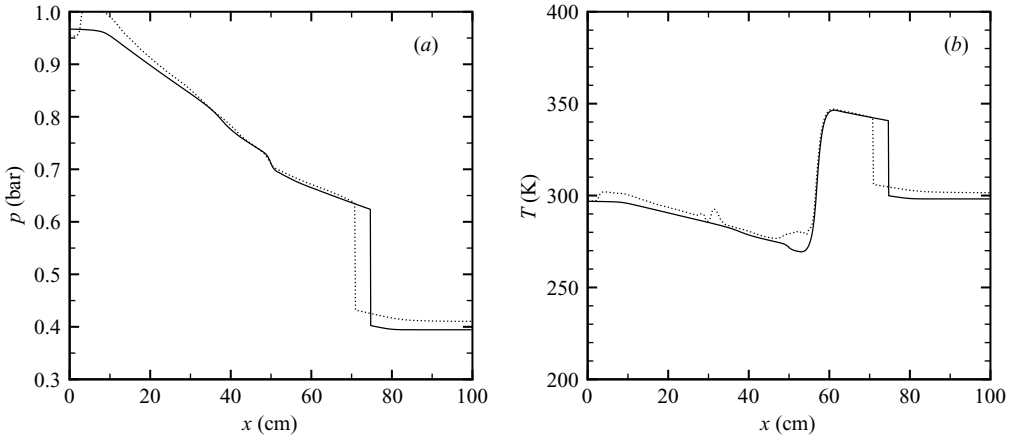


FIGURE 5. (*a*) The pressure and (*b*) the temperature profiles along the tube at 6.5 ms. Dry nitrogen: solid line; humid nitrogen: dotted line.

heat release caused by condensation, pressure and temperature in the humid nitrogen case are higher than in the dry nitrogen case. As shown in the space–time diagram of figure 3, at 2.5 ms, the reflected shock has already intersected the contact surface and the interaction between the reflected shock and the contact surface results in a weak right-running shock wave, which is also captured by the numerical method. The weak shock wave can be seen in figure 4 near the endwall of LPS. The evaporation process has a considerable influence on the temperature profiles, as is shown in figure 5 for $t = 6.5$ ms. The temperature in humid nitrogen with evaporation is close to that in dry nitrogen because at $t = 6.5$ ms, evaporation has consumed most of the latent heat released during condensation. However, phase transition affects the velocity of the shock. It can be seen in figure 5 that the position of the main shock in the case with condensation ($x_{shock} \approx 0.7$ m) is different from that in the dry case ($x_{shock} \approx 0.75$ m).

Now we will study the process of phase transition in more detail. As shown in figure 6, the contours of the liquid mass fraction, the saturation ratio, the number

https://doi.org/10.1017/S0022112005007809 Published online by Cambridge University Press

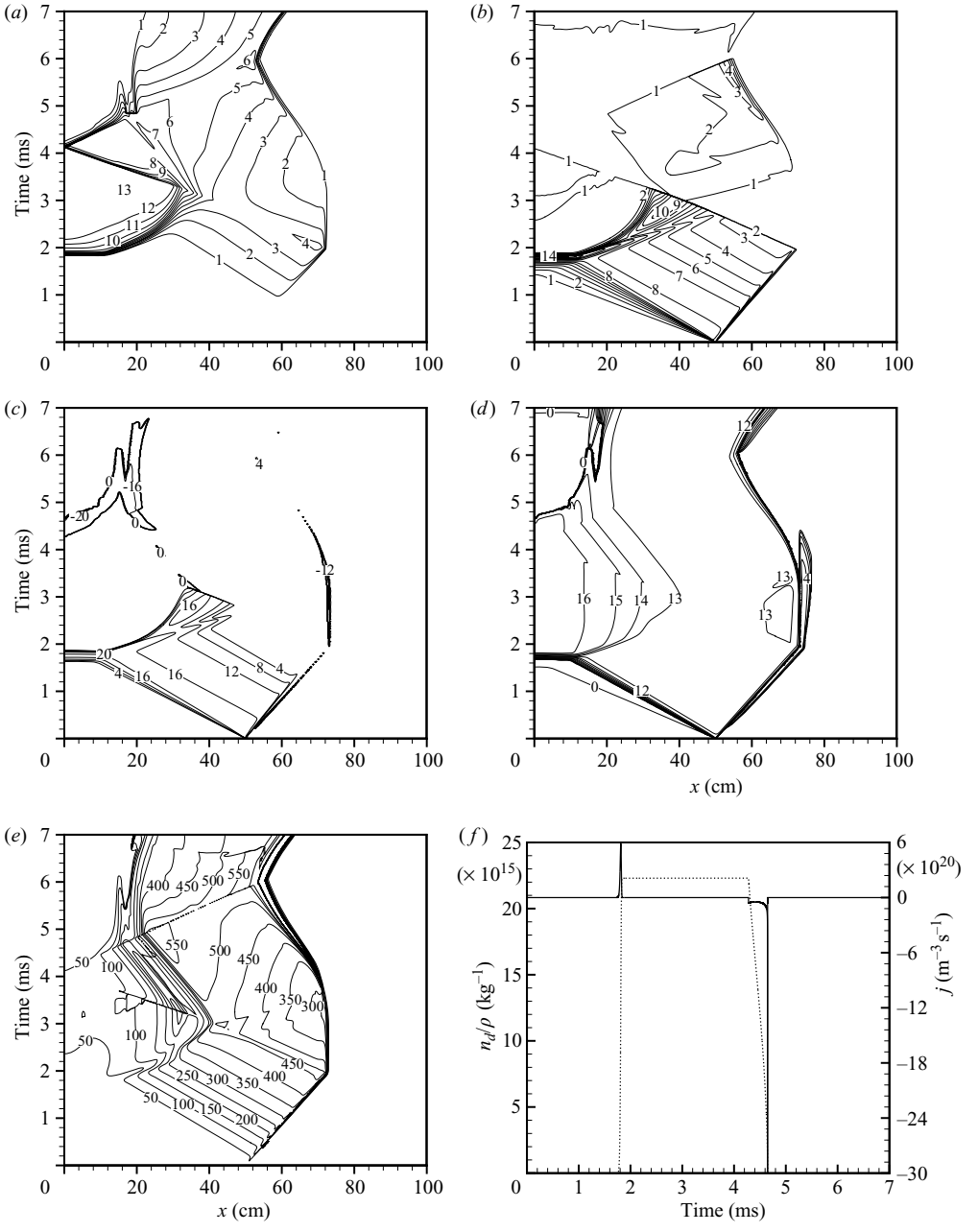


FIGURE 6. The closed shock tube problem with humid nitrogen. Space–time diagrams: (*a*) contours of the liquid mass fraction, (*b*) the saturation ratio, (*c*) the (de-)nucleation rate, (*d*) the number density of droplets and (*e*) the modal radius. The number density of droplets (dotted) and the (de-)nucleation rate (solid) histories at the end-wall of the HPS are shown in (*f*). For initial conditions, see text.

density of droplets, the (de-)nucleation rates and the modal radius for this closed shock tube problem in humid nitrogen are plotted as space–time diagrams.

When the primary expansion wave passes the mixture in the HPS, the temperature drops rapidly, which results in a rapid increase of saturation ratio from $S < 1$ to

https://doi.org/10.1017/S0022112005007809 Published online by Cambridge University Press

$S \gg 1$. Homogeneous nucleation and subsequently droplet growth take place there as well. Because the nucleation rate is not very high ($J \leqslant 10^{16}\,\mathrm{m^{-3}\,s^{-1}}$), the liquid mass fraction remains small owing to the relatively low number density of the droplets ($n_d/\rho \leqslant 10^{12}\,\mathrm{kg^{-1}}$). The most significant nucleation ($J \geqslant 10^{20}\,\mathrm{m^{-3}\,s^{-1}}$) appears in the zone where the expansion wave reflects against the endwall of the HPS. As a result, the liquid mass fraction increases rapidly from 0 to $g > 0.012$, with a simultaneous decrease of S to 1. This region near the endwall of the HPS is characterized by its high number density of droplets ($n_d/\rho > 10^{16}\ \mathrm{kg^{-1}}$) with very small modal radius ($r_m < 100\,\mathrm{nm}$). The humid gas, sufficiently distant from the HPS endwall, only undergoes the expansion due to the passage of the primary expansion fan. Nucleation rates and droplet number densities remain relatively low, which leads to relatively large droplets with a modal radius larger than 450 nm. The passage of the shock wave reflected from the LPS endwall quenches the nucleation process instantaneously. Far away from the HPS endwall, the droplets shrink while significant 'de-nucleation' does not occur owing to the 'large' droplet diameters. Close to the endwall, however, the droplet cloud is compressed twice. The droplets are so small there that a strong de-nucleation is found, which results in a sharp decrease of g, n_d/ρ and r_m.

The history of the number density of droplets and the (de-)nucleation rates at $x = 0.5\,\mathrm{mm}$ from the endwall of the HPS are also shown in figure 6(f). The number density n_d/ρ increases rapidly when strong nucleation takes place owing to the passage of the expansion wave reflected from the endwall of the HPS. The passage of shock waves leads to de-nucleation which results in a decrease of n_d/ρ. The δ-function shape of the de-nucleation rate is a consequence of the Kelvin effect, since the Kelvin number becomes very high as $r \to 0$.

It should be noted that in figure 6(c) there is also de-nucleation found around the contact surface. This is not physical, but an artefact caused by the truncation error of the numerical scheme. This truncation error is of second order in terms of grid size and of time step, so that it can be made arbitrarily small by mesh refinement and by choosing a smaller time step. This artificial de-nucleation is a local effect and has no strong influence on the remainder of the flow field.

6. Phase transition in a pulse-expansion wave tube

The so-called pulse-expansion wave tube (PEWT) (Looijmans & van Dongen 1997), designed to study nucleation and droplet growth, is employed to validate the new method. PEWT, one of the modern facilities to study homogeneous nucleation experimentally, is based on the so-called nucleation pulse principle, originating from Allard & Kassner (1965). The gas–vapour mixture of interest is brought in a supersaturated state during a very short time Δt, the so-called nucleation pulse, such that an appreciable number of critical nuclei are formed. After this pulse, the saturation ratio is reduced, but still larger than unity. Therefore, the nucleation process is effectively quenched, but the droplets formed all start to grow simultaneously to macroscopic sizes. The essential characteristic of the nucleation pulse method is that nucleation, i.e. the birth of droplets, and the droplet growth process are separated in time. As a consequence, the droplet cloud formed is almost monodisperse, which greatly facilitates the characterization of the cloud in terms of the radius r of the droplets and the number density n_d. The monodispersity also renders the optical measurement of r and n_d of the cloud by light scattering and extinction reliable and accurate. The nucleation rate J is then obtained by division of the droplet number density by the time duration of the pulse, i.e. $J = n_d/\Delta t$.

https://doi.org/10.1017/S0022112005007809 Published online by Cambridge University Press

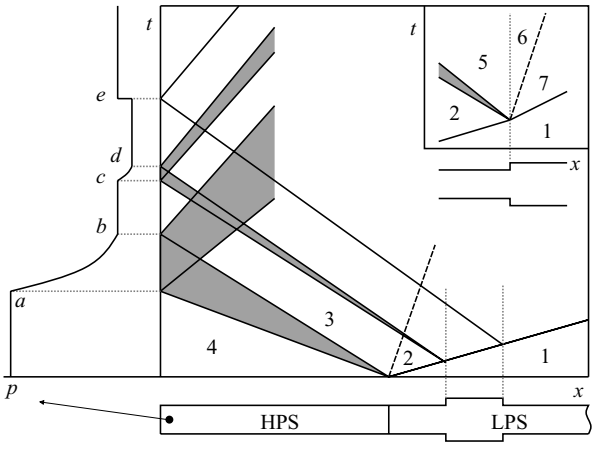


FIGURE 7. Right: x–t plot with schematic wave patterns in the pulse-expansion wave tube. Left-hand side: resulting pressure history at the endwall of the HPS. Inset: enlargement of the wider section of the LPS. The numbers indicate different regions separated by shock wave, contact surface, expansion wave and waves from the interaction between the shock wave with the wider part of the LPS. The pulse is between cd and e.

6.1. *Experimental set-up*

6.1.1. *Pulse-expansion wave tube*

The pulse-expansion wave tube is a high-pressure cylindrical ($p_{max} = 100$ bar, diameter $D = 36$ mm) shock tube, with a fast diaphragm-opening mechanism (opening time less than 0.1 ms). The high-pressure part acts as the test section. The plane of observation is at a short distance from the endwall of the high-pressure section (5 mm in our experiments). A schematic view of the tube and the corresponding space–time diagram is shown in figure 7.

The tube consists of a stainless steel HPS (length $L = 1.26$ m) and an aluminium LPS with a length that can be varied between 5 and 9 m. Details are given in Looijmans & van Dongen (1997). The test gas–vapour mixture is introduced into the high-pressure section, while the LPS is kept at a lower-pressure level. Opening of the diaphragm causes an expansion wave to travel to the left into the HPS, causing the vapour to move to the right. Simultaneously, a contact surface and a shock wave (starting shock) move to the right into the LPS. The expansion wave reflects from the closed endwall of the HPS (a–b) which decelerates the gas particles to the stagnant condition. The gas–vapour mixture near the endwall is thus first isentropically expanding to a first level of supersaturation (state b) chosen such that no appreciable nucleation yet occurs. The nucleation pulse (d–e) is generated through a local wider part in the LPS, close to the diaphragm, and will be explained further below. The test time for observing droplet growth is restricted by the arrival of the starting shock wave, reflected from the endwall of the LPS. The most important waves are indicated in the x–t diagram of figure 7, that also shows the expected pressure history at the endwall of the tube.

The essential part of this PEWT is the wider part, which has a length of 15 cm and a diameter of 41 mm, positioned in the LPS at a distance of 14 cm from the diaphragm. When the starting shock wave passes the entrance of this part, owing to the sudden increase in cross-sectional area, the shock wave decreases in strength and a weak expansion wave is generated, which travels to the left into the HPS.

https://doi.org/10.1017/S0022112005007809 Published online by Cambridge University Press

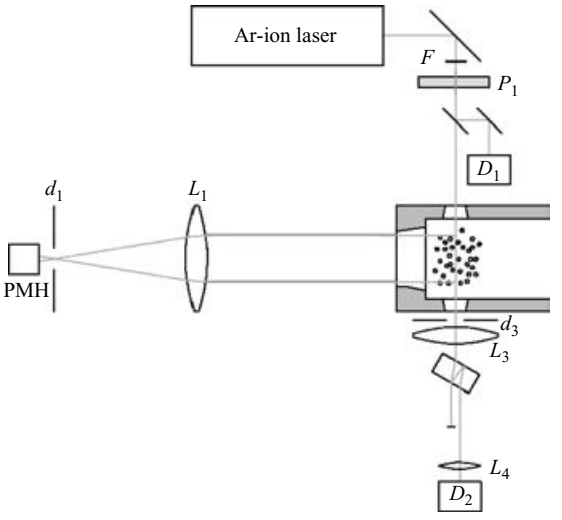


FIGURE 8. Schematic view of the optical set-up at the observation plane. PMH, red extended photomultiplier, $d_{1,3}$, diaphragm; $L_{1,3,4}$, lens; $D_{1,2}$, photodiode; P_1, polarizer; F, filter.

This expansion wave will decrease the pressure in the HPS further, the depth of the decrease depending on the strength of the expansion, determined by the relative area increase of the wider part of the tube. When the transmitted shock wave hits the exit of the wider section, a weak shock wave is produced owing to the sudden reduction of the cross-sectional area. This weak shock wave also travels to the left and results in an abrupt increase of the pressure in the HPS. In this way, a pulse-shaped pressure signal is formed. After the pulse, the pressure in the HPS will recover to the value prior to the pulse. The duration of the pulse (d–e in the endwall pressure history) depends on the length of the wider part of the LPS.

In normal PEWT operation, it is extremely important to know the thermodynamic state at which the nucleation and droplet growth rates are measured. Therefore, the temperature and the saturation ratio of the gas have to be determined in the nucleation pulse. In each experiment, the initial pressure p_0, initial temperature T_0, initial molar vapour fraction $y_{v,0}$ and pressure history $p(t)$ at the endwall of the HPS are measured. By applying the isentropic flow assumption, the temperature in the nucleation pulse at $t = t_p$ can be derived from the measured pressure $p(t)$, for a calorically perfect gas, as:

$$\frac{T(t_p)}{T_0} = \left(\frac{p(t_p)}{p_0}\right)^{(\gamma-1)/\gamma}. \tag{6.1}$$

Once the history of the temperature and pressure during the pulse have been obtained, the saturation ratio S in the nucleation pulse at time t_p can be determined from:

$$S = \frac{p_v(t_p)}{p_s(T(t_p))}. \tag{6.2}$$

In practice, p, T and S are averaged over the nucleation pulse period.

6.2. *Optical droplet detection*

The droplets at the observation plane are detected by an optical set-up. A schematic view of this set-up is shown in figure 8. An argon-ion laser beam is first split into

https://doi.org/10.1017/S0022112005007809 Published online by Cambridge University Press

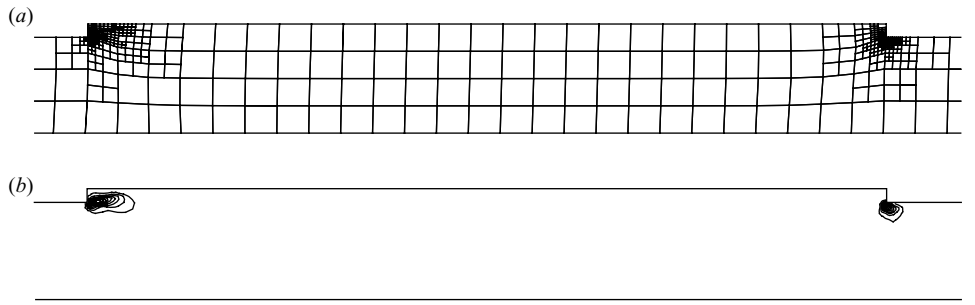


FIGURE 9. (*a*) Refined mesh and (*b*) azimuthal vorticity contours in the wider part at $t = 0.7$ ms.

two parts: a reference beam, detected by photodiode D_1, and a beam entering the tube through the sidewall. The latter passes through the cloud of droplets and will result in two effects: light scattering and light extinction. The transmitted light is recorded by photodiode D_2. The light scattered by the droplets (in the observation plane) at an angle of 90° is detected by a red extended photomultiplier PMH. A detailed description of this optical set-up can be found in Peeters (2002).

Three optical signals are measured during the experiment: the reference signal, the transmission signal and the 90° light-scattering signal. The reference signal is used to filter out the noise, caused by the laser, in the transmitted and scattered light. By interpreting the extrema of the scattering intensity, droplet sizes at different times can be determined by applying Mie theory (Van De Hulst 1981; Mishchenko, Travis & Mackowski 1996). Combining light scattering with light extinction, the droplet number density, n_d, can be accurately obtained at each time corresponding to an extremum in the plot of the intensity of the scattered light.

6.3. *Results*

Experimental and numerical results will be shown for water–helium as test gas and helium as low-pressure gas. The length of the LPS is 4.39 m. Initially, the pressure in the HPS is 1.775 bar, the initial mole fraction of water vapour is 0.00325 ($S_{ini} = 0.2$) and the pressure in the LPS is 1.10 bar. To reduce the computing time, the flow is assumed to be axi-symmetric. The initial mesh has 2851 cells with a size of about 6 mm × 6 mm. The refinement level is set to 4 so that the minimum cell size is 0.375 mm × 0.375 mm. Part of the mesh of the wider section after local refining is shown in figure 9. The azimuthal vorticity distribution in this section is also shown. After the passage of the shock wave, we observe vortex shedding from the sharp corners. It should be noted that the shape of the wider part is essential for the nucleation pulse, so that a study of the influence of different shapes of the wider part using the present numerical method is useful for designing and improving the PEWT.

For comparison, pressure histories from simulation and experiment taken at a distance of 5 mm from the endwall of the HPS are shown in figure 10 for the same initial state, i.e. pressure in the HPS, temperature and composition. A good agreement is found for the expansion wave and the nucleation pulse. Also the small waves due to the interaction of the expansion wave with the wider part are reasonably described at $t = 4$–6 ms. At $t \approx 9$ ms, the starting shock wave reflected from the LPS endwall arrives at the measuring position. There are discrepancies of strength and speed of the reflected shock wave, which are due to viscous effects and of the flow resistances near

https://doi.org/10.1017/S0022112005007809 Published online by Cambridge University Press

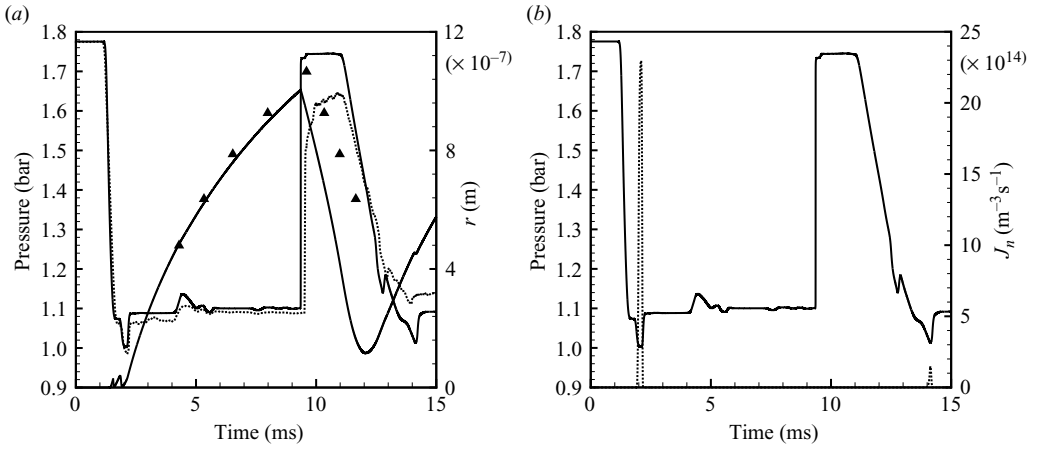


FIGURE 10. (*a*) Droplet radius and pressure (solid line) from numerical simulation, and the measured pressure (dotted line) at a distance of 5 mm from the endwall of the HPS. The experimental droplet radius is given by the solid triangles. (*b*) Histories of nucleation rate (dotted line) and pressure (solid line) from the numerical simulation at a distance of 5 mm from the endwall of the HPS. Initial conditions: $p_{HPS} = 1.7754$ bar, $p_{LPS} = 1.1$ bar; mole fraction of water $y_{v0} = 0.00325$; carrier gas: helium; length of the LPS: 4.39 m.

the diaphragm section, that have been neglected in our model. It should be noted that the PEWT is designed for high pressure experiments (> 5 bar). For such conditions the discrepancies are much smaller (see Looijmans & van Dongen 1997; Luijten, Peeters & van Dongen 1999). Results for the mean droplet size and for the nucleation rate are also shown in figure 10. The averaged nucleation rate in the nucleation pulse determined from the experimental results is 2.2×10^{15} m^{-3} s^{-1}. The numerical simulation confirms that significant nucleation occurs in the nucleation pulse only and that the nucleation rates reached are found in the experiment. Droplet growth is accurately described by the model, with droplets attaining a maximum radius of about 1 μm. After some time, the shock wave reflecting from the endwall of the LPS arrives at the plane of observation, causing the droplet sizes to decrease rapidly owing to evaporation. Effects of evaporation can be seen in figures 10 and 11. The droplet size starts to decrease owing to the passage of the reflected starting shock wave. The evaporation rate is somewhat overestimated because in the numerical simulation the strength of the reflected shock exceeds the experimental one. In the numerical simulation, the de-nucleation rate, if present, appears to be δ-function shaped owing to the Kelvin effect. All the droplets disappear in a very short time (< 30 μs), which indicates that all droplets have almost the same size. This also proves the effectivity of the nucleation pulse principle in creating a monodisperse droplet cloud.

7. Summary and conclusions

We have studied the underlying physical principles of Hill's method of moments in detail and developed a physical model for compressible flows with phase transition in which all the processes of phase transition, i.e. nucleation, droplet growth, droplet evaporation and de-nucleation, are correctly described. The rate at which droplets are passing the lower boundary of the droplet size distribution function in size space is identified with the nucleation rate or de-nucleation rate for condensation or

https://doi.org/10.1017/S0022112005007809 Published online by Cambridge University Press

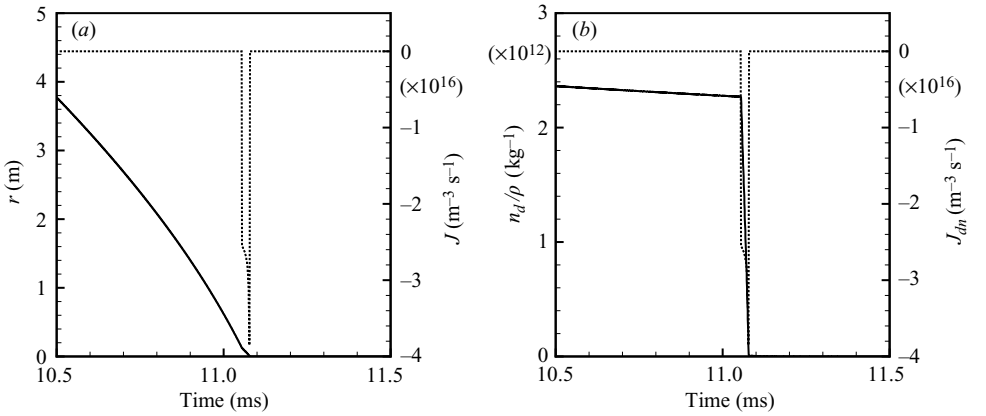


FIGURE 11. (*a*) The droplet radius (solid line) decreases with time. Since the cloud is monodisperse, the de-nucleation rate (dotted line) is δ-function shaped. (*b*) Number density of droplets (solid line) and de-nucleation rate (dotted line). The initial pressure is 1.7254 bar in the HPS and 1.059 bar in the LPS. The water mole fraction y_{v0} is 0.00325. The length of the LPS is 4.39 m.

evaporation, respectively. For the case of condensation, the nucleation rate directly follows from nucleation theory. The evaporation process is described as a shift towards smaller radii of the undistorted size distribution function in size space. The distribution function is cutoff at droplet size zero. The rate at which this lower limit is passed, following a Lagrangian trajectory, is the de-nucleation rate. To evaluate this de-nucleation rate, a shape of the size distribution function has to be adopted.

The effects of phase transition are demonstrated in the numerical simulation of the flow in a closed shock tube with humid nitrogen as the driver gas. In the shock tube, expansion waves and shock waves are generated, which reflect at the endwalls and which interact, leading to a rather complex flow field. The shock speed and the time-dependent values of pressure, temperature, wetness, etc. are affected by the condensation and evaporation processes. Especially, the de-nucleation process results in a decrease of the number density of droplets, and causes the liquid mass fraction to decrease to zero eventually as a result of the passage of a shock.

The so-called pulse-expansion wave tube, designed to study nucleation and droplet growth, is employed to validate the new method. In the pulse-expansion wave tube, a gas/vapour mixture is subjected to a strong expansion wave followed by a pulse-shaped smaller second expansion. In this way, nucleation (during the pulse) and droplet growth (after the pulse) are separated in time. A number of experiments in water–helium have been carried out, yielding information on gas pressure, droplet size and droplet number density. All the phenomena observed experimentally are found numerically. Deviation of results of numerical simulation and results of experiment are caused by experimental non-idealities, such as pressure losses near the diaphragm section and by friction not taken into account in the computational model.

This research was carried out within the framework of the J. M. Burgerscentrum, Research School for Fluid Mechanics of the Netherlands. Dr Mingyu Sun and Professor K. Takayama provided the source code of VAS2D, which is gratefully acknowledged. The authors are very much indebted to Dr P. Peeters, D. Labetski and V. Holten for their most valuable advice and assistance related to PEWT operation.

https://doi.org/10.1017/S0022112005007809 Published online by Cambridge University Press

Appendix A. Physical properties

This Appendix lists the physical properties used in the numerical simulations.

Nitrogen

$m = 28.013$	$\mathrm{kg\,kmol^{-1}}$	Reid, Prausnitz & Poling (1987)
$R_a = 296.81$	$\mathrm{J\,kg^{-1}\,K^{-1}}$	Ražnjewić (1977)
$C_{pa} = 1041$	$\mathrm{J\,kg^{-1}\,K^{-1}}$	Ražnjewić (1977)
$C_{va} = 743.57$	$\mathrm{J\,kg^{-1}\,K^{-1}}$	Ražnjewić (1977)
$k = 2.55 \times 10^{-2}(T/295)^{0.838}$	$\mathrm{W\,m^{-1}K^{-1}}$	Touloukian, Liley & Saxena (1970)
$\mu = 17.6 \times 10^{-6}(T/295)^{0.767}$	$\mathrm{kg\,m^{-1}s^{-1}}$	Touloukian *et al.* (1970)

Helium

$m = 4.003$	$\mathrm{kg\,kmol^{-1}}$	Reid *et al.* (1987)
$R_a = 2077.077$	$\mathrm{J\,kg^{-1}\,K^{-1}}$	Reid *et al.* (1987)
$C_{pa} = 5192.69$	$\mathrm{J\,kg^{-1}\,K^{-1}}$	Reid *et al.* (1987)
$C_{va} = 3115.62$	$\mathrm{J\,kg^{-1}\,K^{-1}}$	Reid *et al.* (1987)
$k = -2.449 \times 10^{-2} + 1.124 \times 10^{-3}T$ $-2.929 \times 10^{-6}T^2 + 4.493 \times 10^{-9}T^3$ $-2.518 \times 10^{-12}T^4$	$\mathrm{W\,m^{-1}\,K^{-1}}$	Hung, Krasnopoler & Katz (1989)
$\mu = 0.698k/C_{pa}$	$\mathrm{kg\,m^{-1}\,s^{-1}}$	

Water vapour

$m = 18.015$	$\mathrm{kg\,kmol^{-1}}$	Reid *et al.* (1987)
$R_v = 461.52$	$\mathrm{J\,kg^{-1}\,K^{-1}}$	Ražnjewić (1977)
$C_{pv} = 1859$	$\mathrm{J\,kg^{-1}\,K^{-1}}$	Ražnjewić (1977)
$C_{vv} = 1397.5$	$\mathrm{J\,kg^{-1}\,K^{-1}}$	Ražnjewić (1977)
$k = 7.341 \times 10^{-3} - 1.013 \times 10^{-5}T$ $+ 1.801 \times 10^{-7}T^2 - 9.100 \times 10^{-11}T^3$	$\mathrm{W\,m^{-1}K^{-1}}$	Reid *et al.* (1987)
$\mu = (1.823 \times 10^{-6}\sqrt{T}/(1 + 673/\sqrt{T}))$	$\mathrm{kg\,m^{-1}s^{-1}}$	Landolt–Börnstein (1962)

Latent heat of water

The latent heat of condensation or evaporation is taken from Sonntag & Heinze (1982):

$$L(T) = R_v(A_{10}T^2 + 2A_{11}T^3 + B_1T - C_0), \quad [\mathrm{J\,kg^{-1}}] \tag{A 1}$$

with: $A_{10} = -2.7246 \times 10^{-2}\ \mathrm{K^{-1}}$, $A_{11} = 1.6853 \times 10^{-5}\ \mathrm{K^{-2}}$, $B_1 = 2.4576$, $C_0 = -6094.4642$ K. The reference temperature for determining L_0 and L_1 is 273.15 K.

Saturated vapour pressure for water

The vapour pressure in Pa (T in K) is taken from Vargaftik (1975):

$$p_s = 610.8\exp[-5.1421\ln(T/273.15) - 6828.77(1/T - 1/273.15)]. \tag{A 2}$$

Density of liquid water

$$\rho_l(t) = \begin{cases} \dfrac{A_0 + A_1t + A_2t^2 + A_3t^3 + A_4t^4 + A_5t^5}{1 + B_0t}, & \text{for } t \geqslant 0\,^\circ C \\ A_6 + A_7t + A_8t^2, & \text{for } t < 0\,^\circ C, \end{cases} \tag{A 3}$$

with ρ_l in $\mathrm{kg\,m^{-3}}$, t in °C and with (Pruppacher & Klett 1978):

https://doi.org/10.1017/S0022112005007809 Published online by Cambridge University Press

$A_0 = 999.84$	$\mathrm{kg\,m^{-3}}$	$A_1 = 8.224944$	$\mathrm{kg\,m^{-3}\ K^{-1}}$
$A_2 = -7.92221\times10^{-3}$	$\mathrm{kg\,m^{-3}\ K^{-2}}$	$A_3 = -55.44846\times10^{-6}$	$\mathrm{kg\,m^{-3}\ K^{-3}}$
$A_4 = 149.7562\times10^{-9}$	$\mathrm{kg\,m^{-3}\ K^{-4}}$	$A_5 = -393.2952\times10^{-12}$	$\mathrm{kg\ m^{-3}\ K^{-5}}$
$A_6 = 999.84$	$\mathrm{kg\,m^{-3}}$	$A_7 = 0.086$	$\mathrm{kg\,m^{-3}\ K^{-1}}$
$A_8 = -0.0108$	$\mathrm{kg\,m^{-3}\ K^{-2}}$	$B_0 = 18.159725\times10^{-3}$	$\mathrm{K^{-1}}$

Binary diffusion coefficients

water–nitrogen (Reid *et al.* 1987):

$D = 24.5 \times 10^{-6}(T/295)^{2.085}/p$ in $\mathrm{m^2\,s^{-1}}$, with p in bar

water–helium (Vargaftik 1975):

$D = 398.38 \times 10^{-7} T^{1.75}/p$ in $\mathrm{m^2\,s^{-1}}$, with p in bar

Surface tension of liquid water

For the surface tension, we adopt the following fit to experimental data (Lamanna 2000):

$$\sigma^{LD}(T) = \begin{cases} 8.52000 \times 10^{-2} - 3.54236 \times 10^{-4} T \\ +3.50835 \times 10^{-6} T^2 - 8.71691 \times 10^{-9} T^3, & \text{for } T < 250.0\ \mathrm{K}, \\ (76.1 + 0.155(273.15 - T)) \times 10^{-3}, & \text{for } T \geqslant 250.0\ \mathrm{K}, \end{cases} \tag{A 4}$$

with σ in $\mathrm{N\,m^{-1}}$.

Appendix B. Definition of Nusselt numbers

During droplet growth there is a net flow of mass $\dot{M}$ and of energy $\dot{E}$ between the surrounding mixture and the droplet. We first specify expressions for these flows in two limiting cases.

Continuum limit

$$\left.\begin{aligned} \dot{M}^{ct} &= 4\pi r \left(\frac{D_m}{R_v T_m}\right)(p_v^{eq} - p_v), \\ \dot{E}^{ct} &= \tfrac{1}{2}(T_d + T)\dot{M}^{ct} C_{pv} + 4\pi k_m r (T_d - T) \\ &\approx \dot{M}^{ct} h_{vs} + \dot{H}^{ct}, \end{aligned}\right\} \tag{B 1}$$

where h_{vs} is the vapour enthalpy at equilibrium, and $\dot{H}^{ct}$ is the heat flow from the droplet to the surrounding. Note that p_v^{eq} is a function of the droplet temperature T_d and the droplet radius r: $p_v^{eq}(T_d, r)$.

Free molecular limit

$$\left.\begin{aligned} \dot{M}^{fm} &= 4\pi r^2 \left(\frac{p_v^{eq}}{\sqrt{2\pi R_v T_d}} - \frac{p_v}{\sqrt{2\pi R_v T}}\right), \\ \dot{E}^{fm} &= 4\pi r^2 \left[\frac{p_v(C_{pv} - \frac{1}{2}R_v)}{\sqrt{2\pi R_v T}} + \frac{p_a(C_{pa} - \frac{1}{2}R_a)}{\sqrt{2\pi R_a T}}\right](T_d - T) \\ &\quad + \dot{M}^{fm}\left(C_{pv} - \tfrac{1}{2}R_v\right) T_d \\ &\approx \dot{H}^{fm} + \dot{M}^{fm} h_{vs}. \end{aligned}\right\} \tag{B 2}$$

https://doi.org/10.1017/S0022112005007809 Published online by Cambridge University Press

Expressions for the Nusselt numbers in the limiting cases follow by a comparison of (B 1), (B 2) and (2.9).

In the formulation above, the droplet temperature T_d is unknown and has to be calculated from the energy conservation for the droplet:

$$\dot{E} = \frac{\mathrm{d}}{\mathrm{d}t}(M_d h_d) = \dot{M} h_d + M_d \dot{h}_d, \tag{B 3}$$

where h_d and M_d denote the droplet enthalpy and mass, respectively.

By using the quasi-steady 'wet-bulb approximation', which implies that the last term in (B 3) is neglected, (B3) can be rewritten as:

$$\dot{E} = -\dot{M} L + \dot{M} h_{vs}, \tag{B 4}$$

with L the latent heat of condensation.

Using (B 4), (B 2) or (B 1), we find a simplified version of the wet-bulb equation:

$$\dot{H} = -\dot{M} L. \tag{B 5}$$

Equations (B 5) and (2.9) provide an implicit formula to calculate the droplet temperature T_d:

$$Nu_{\dot{H}} k_m (T - T_d) = -Nu_{\dot{M}} L(T_d) D_{mod} \frac{p_v - p_v^{eq}}{p}. \tag{B 6}$$

Once the droplet temperature T_d has been determined, the droplet growth rate directly follows from:

$$\frac{\mathrm{d}r}{\mathrm{d}t} = \frac{\dot{M}}{\rho_l 4\pi r^2}. \tag{B 7}$$

We observe immediately that for the free molecular limiting case, the growth rate $(\mathrm{d}r/\mathrm{d}t)^{fm}$ is in first-order independent of the droplet radius. There is a weak dependence for small droplets because of the Kelvin effect (see (2.2)). Then in the free molecular limit we have:

$$\left(\frac{\mathrm{d}r}{\mathrm{d}t}\right)^{fm} = \frac{1}{\rho_l}\left(\frac{p_v^{eq}}{\sqrt{2\pi R_v T_d}} - \frac{p_v}{\sqrt{2\pi R_v T}}\right). \tag{B 8}$$

For the continuum limit, it follows that $\mathrm{d}r^2/\mathrm{d}t$ is independent of the droplet radius:

$$\left(\frac{\mathrm{d}r^2}{\mathrm{d}t}\right)^{ct} = \frac{2}{\rho_l}\left(\frac{D_{mod}}{R_v T_m}\right)\left(p_v^{eq} - p_v\right). \tag{B 9}$$

For the transition regime, the Nusselt numbers can be expressed as a combination of the Nusselt numbers for the free molecular and the continuum regimes:

$$Nu^{tr} = \frac{Nu^{ct} Nu^{fm}}{Nu^{ct} + Nu^{fm}}. \tag{B 10}$$

This formula shows the correct asymptotic behaviour for both small and large Kn numbers, i.e. $Nu^{tr} \to Nu^{fm}$ as $Kn \to \infty$, and $Nu^{tr} \to Nu^{ct}$ as $Kn \to 0$.

Appendix C. Evaluation of explicit method for the droplet temperature

The absolute relative error $|\delta_2|$ is plotted as a function of the saturation ratio S and the gas temperature T in figures 12 to 14. The error parameter δ_2 is defined in

https://doi.org/10.1017/S0022112005007809 Published online by Cambridge University Press

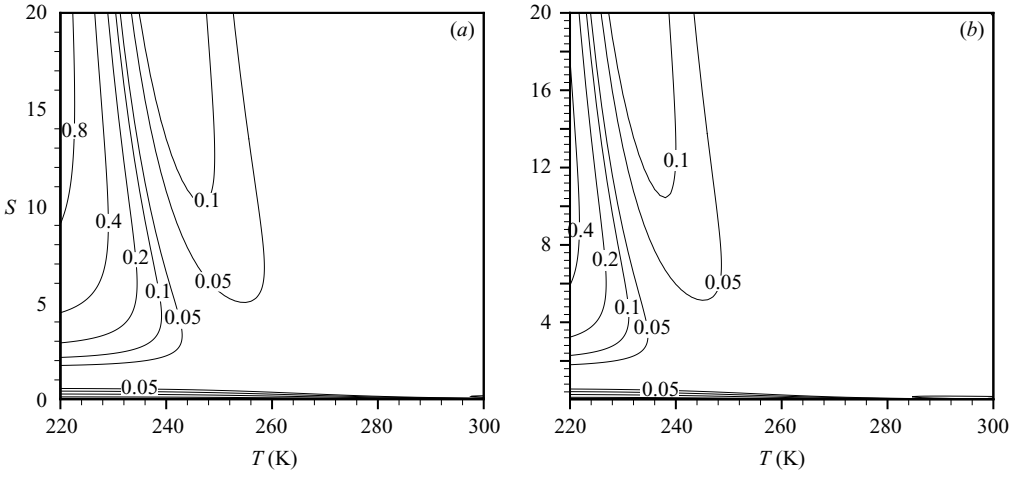


FIGURE 12. The relative error $|\delta_2|$ in $(T_d/T-1)$ for the explicit droplet growth expression. Droplet radius: 0.1 μm. Pressure: (*a*) 1 bar; (*b*) 0.5 bar.

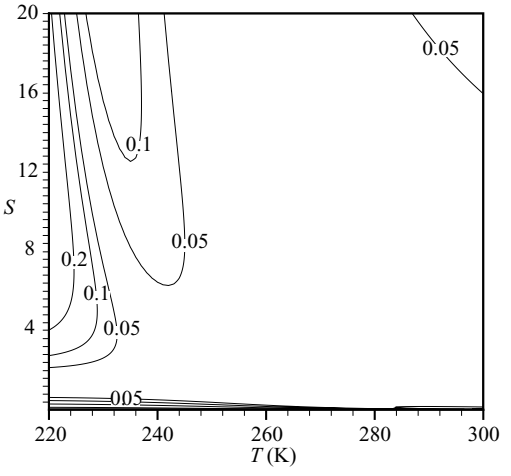


FIGURE 13. The relative error $|\delta_2|$ in $(T_d/T-1)$ for the explicit droplet growth expression. Droplet radius: 0.01 μm. Pressure: 0.5 bar.

terms of the driving force of droplet growth T_d/T as:

$$\delta_2 = \frac{(T_d/T-1)_{explicit}}{(T_d/T-1)_{implicit}} - 1. \tag{C 1}$$

In figure 12, the absolute relative error $|\delta_2|$ is plotted for a droplet radius of 0.1 μm and a pressure of 1 bar and 0.5 bar. For the mixture temperature higher than 240 K, the relative error is smaller than 5 %. Comparing figures 12 and 13, we see that the lower the pressure and the smaller the droplet radius, the smaller the error. For lower temperatures and higher saturation ratios, it appears that using the implicit method is inevitable.

In the case of evaporation, the pressure and temperature are higher. In addition, during evaporation, the saturation ratio is smaller than unity. In figure 14, the relative error is shown for a pressure of 1.5 bar and a droplet radius of 0.1 μm for a temperature

https://doi.org/10.1017/S0022112005007809 Published online by Cambridge University Press

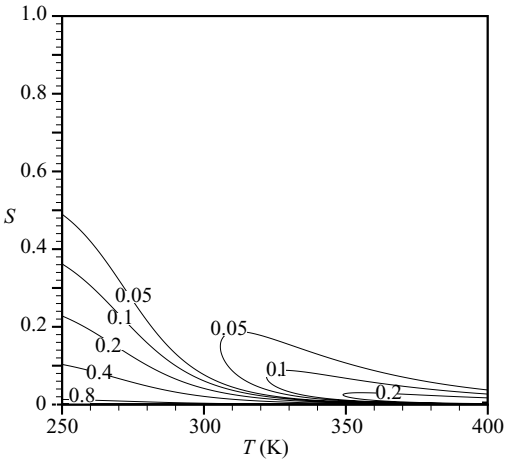


FIGURE 14. The relative error $|\delta_2|$ in $(T_d/T - 1)$ of the explicit expression for droplet evaporation. Droplet radius: 0.1 μm. Pressure: 1.5 bar.

range ($250 \leqslant T \leqslant 400$) and for $S < 1$. For $T > 300\,\mathrm{K}$ and $S > 0.2$, the error is smaller than 5 %. However, it should be noted that for the strong evaporation associated with strong shock waves, the saturation ratio is very small (for instance $S < 0.1$) and in that case the explicit method results in large errors (> 10 %) in estimating the temperature of the droplets T_d. Adopting the implicit method is then again mandatory.

REFERENCES

ABRAHAM, F. F. 1974 *Homogeneous Nucleation Theory*. Academic.

ADAM, S. & SCHNERR, G. H. 1997 Instabilities and bifurcation of nonequilibrium two-phase flows. *J. Fluid Mech.* **348**, 1–28.

ALLARD, E. F. & KASSNER, J. L. 1965 New cloud-chamber method for determination of homogeneous nucleation rates. *J. Chem. Phys.* **42**, 1401–1405.

BARRETT, J. C. & CLEMENT, C. F. 1988 Growth rates for liquid droplets. *J. Aerosol Sci.* **19**, 223–242.

BROWN, D. P., RUBIN, S. G. & BISWAS, P. 1995 Development and demonstration of a two/three dimensional coupled flow and aerosol model. In *13th AIAA Applied Aerodynamics Conference*. AIAA.

DELALE, C. F., LAMANNA, G. & VAN DONGEN, M. E. H. 2001 On stability of stationary shock waves in nozzle flows with homogeneous condensation. *Phys. Fluids* **13**, 2706–2719.

FRIEDLANDER, S. K. 1977 *Smoke, Dust and Haze*. John Wiley.

GYARMATHY, G. 1963 Zur Wachstumsgeschwindigkeit kleiner Flüssigkeitstropfen in einer übersättigten Atmosphäre. *Z. Angew. Math. Phys.* **14**, 280–293.

GYARMATHY, G. 1982 The spherical droplet in gaseous carrier streams: review and synthesis. In *Multiphase Science and Technology*, vol. 1. Springer.

HAGMEIJER, R. 2004 Equivalence of two different integral representations of droplet distribution moments in condensing flows. *Phys. Fluids* **16**, 176–183.

HILL, P. G. 1966 Condensation of water vapour during supersonic expansion in nozzles. *J. Fluid Mech.* **25**, 593–620.

HUBBARD, G. L., DENNY, V. E. & MILLS, A. F. 1975 Droplet evaporation: effects of transients and variable properties. *Intl J. Heat Mass Transfer* **18**, 1003–1008.

HUNG, C. H., KRASNOPOLER, M. J. & KATZ, J. L. 1989 Condensation of a supersaturated vapor. VIII. The homogeneous nucleation of *n*-nonane. *J. Chem. Phys.* **90**, 1856–1865.

KASHCHIEV, D. 2000 *Nucleation: Basic Theory with Applications*. Butterworth–Heineman.

LAMANNA, G. 2000 On nucleation and droplet growth in condensing nozzle flows. PhD thesis, Eindhoven University of Technology.

https://doi.org/10.1017/S0022112005007809 Published online by Cambridge University Press

Landolt, H. & Börnstein, R. 1962 *Zahlenwerte und Funktionen*, vol. 2 part 8. Springer.

van Leer, B. 1984 On the relation between the upstream-differencing schemes of Godunov, Engquist–Osher and Roe. *SIAM J. Sci. Statist. Comput.* **5**, 1–20.

Looijmans, K. N. H. & van Dongen, M. E. H. 1997 A pulse-expansion wave tube for nucleation studies at high pressures. *Exps. Fluids* **23**, 54–63.

Luijten, C. C. M., Peeters, P. & van Dongen, M. E. H. 1999 Nucleation at high pressure. II: wave tube data and analysis. *J. Chem. Phys.* **111**, 8535–8544.

Luo, X. 2004 Unsteady flows with phase transition. PhD thesis, Eindhoven University of Technology, Eindhoven, The Netherlands.

Luo, X. & van Dongen, M. E. H. 2003 On unsteady flows with phase transition. *Comput. Fluid Dyn. J.* **12**, 309–315.

Mashayek, F. 1998 Direct numerical simulations of evaporating droplet dispersion in forced low-Mach-number turbulence. *Intl J. Heat Mass Transfer* **41**, 2601–2617.

Mason, B. J. 1953 The growth of ice crystals in a supercooled water cloud. *Q. J. R. Met. Soc.* **79**, 104–111.

Matsuo, K., Kawagoe, S., Sonoda, K. & Setoguchi, T. 1983 Oscillations of Laval nozzle flow with condensation (part 1). *Bull. JSME* **26**, 1556–1562.

Matsuo, K., Kawago, S., Sonoda, K. & Setoguchi, T. 1985 Oscillations of Laval nozzle flow with condensation (part 2). *Bull. JSME* **28**, 88–93.

Miller, R. & Bellan, J. 1999 Direct numerical simulation of a confined three-dimensional gas mixing layer with one evaporating hydrocarbon-droplet laden stream. *J. Fluid Mech.* **384**, 293–338.

Miller, R., Harstad, K. & Bellan, J. 1998 Evaluation of equilibrium and non-equilibrium evaporation models for many droplet gas–liquid flow simulations. *Intl J. Multiphase Flow* **24**, 1025–1055.

Mishchenko, M. I., Travis, L. D. & Mackowski, D. W. 1996 T-matrix computations of light scattering by nonspherical particles: a review. *J. Quant. Spectrosc. Radiat. Transfer* **55**, 535.

Mundinger, G. 1994 Numerische Simulation Instationärer Lavaldüsenströmungen mit Energiezufuhr durch Homogene Kondensation. PhD thesis, Universität Karlsruhe, Germany.

Oran, E. S. & Boris, J. P. 1987 *Numerical Simulation of Reactive Flow*. Elsevier.

Oxtoby, D. W. 1992 Homogeneous nucleation: theory and experiment. *J. Phys. Condens. Matter* **4**, 7627–7650.

Peeters, P. 2002 Nucleation and condensation in gas–vapor mixture of alkanes and water. PhD thesis, Eindhoven University of Technology, Eindhoven.

Peeters, P., Gielis, J. J. H. & van Dongen, M. E. H. 2002 The nucleation behavior of supersaturated water in helium. *J. Chem. Phys.* **117**, 5647–5653.

Peeters, P., Hrubý, J. & van Dongen, M. E. H. 2001*a* High pressure nucleation experiment in binary and ternary mixtures. *J. Phys. Chem.* B **105**, 11 763–11 771.

Peeters, P., Luijten, C. C. M. & van Dongen, M. E. H. 2001*b* Transitional droplet growth and diffusion coefficients. *Intl J. Heat Mass Transfer* **44**, 181–193.

Prast, B. 1997 Condensation in supersonic expansion flows: theory and numerical evaluation. SAI, Eindhoven University of Technology, Eindhoven.

Pruppacher, H. R. & Klett, J. D. 1978 *Microphysics of Clouds and Precipitation*. Reidel.

Put, F. 2003 Numerical simulation of condensation in transonic flows. PhD thesis, University of Twente, Enschede, The Netherlands.

Put, F., Hoeijmakers, H. W. M., Kelleners, P. H. & Lammers, F. A. 2002 Development of a numerical method for simulating transonic multi-phase flows. In *Proc. IUTAM Symposium Transonicum IV*. Kluwer.

Put, F., Kelleners, P. H., Hagmeijer, R. & Hoeijmakers, H. W. M. 2001 Numerical simulation of condensing real gas flows. In *Proc. CFD2001*. ASME PVP vol. 424-1.

Ražnjewić, K. 1977 *Thermodynamische Tabellen*. VDI.

Reid, R. C., Prausnitz, J. M. & Poling, B. E. 1987 *The Properties of Gases and Liquids*. McGraw-Hill.

Sichel, M. 1981 Unsteady transonic nozzle flow with heat addition. *AIAA J.* **19**, 165–177.

Sislian, J. P. & Glass, I. I. 1976 Condensation of water vapor in rarefaction waves: I. Homogeneous nucleation. *AIAA J.* **14**, 1731–1737.

https://doi.org/10.1017/S0022112005007809 Published online by Cambridge University Press

Smolders, H. J. 1992 Non-linear wave phenomena in a gas-vapour mixture with phase transition. PhD thesis, Eindhoven University of technology.

Sonntag, D. & Heinze, D. 1982 Sättigungsdampfdruck- und Sättigungsdampfdichtetafeln für Wasser und Eis. *Tech. Rep*. VEB Deutscher Verlag für Grundstoffindustrie.

Sonntag, R. E., Borgnakke, C. & van Wylen, G. J. 1998 *Fundamentals of Thermodynamics*. Wiley.

Sun, M. 1998 Numerical and experimental studies of shock wave interaction with bodies. PhD thesis, Tohoku University, Sendai, Japan.

Sun, M. & Takayama, K. 1999 Conservative smoothing on an adaptive quadrilateral grid. *J. Comput. Phys*. **150**, 143–180.

Touloukian, Y. S., Liley, P. E. & Saxena, S. C. 1970 *Thermophysical Properties of Matter*. IFI/Plenum.

Van De Hulst, H. C. 1981 *Light Scattering by Small Particles*. Dover.

Vargaftik, N. B. 1975 *Tables on the Thermophysical Properties of Liquids and Gases*, 2nd edn. Wiley.

Wagner, P. E. 1982 Aerosol growth by condensation. In *Aerosol Microphysics*. Springer.

Wegener, P. P. & Cagliostro, D. J. 1973 Periodic nozzle flow with heat addition. *Combust. Sci. Technol*. **6**, 269–277.

Young, J. B. 1993 The condensation and evaporation of liquid droplets at arbitrary Knudsen number in the presence of an inert gas. *Intl J. Heat Mass Transfer* **36**, 2941–2956.

https://doi.org/10.1017/S0022112005007809 Published online by Cambridge University Press